

Interlayer-Exciton Based Nonvolatile Valleytronic Memory

Tong Ye

Huazhong University of Science and Technology

Hongzhi Shen

Huazhong University of Science and Technology

Junwen Ren

Huazhong University of Science and Technology

Dehui Li (✉ dehuili@hust.edu.cn)

Huazhong University of Science and Technology <https://orcid.org/0000-0002-5945-220X>

Article

Keywords: valleytronics, Long-lived interlayer excitons, nonvolatile valleytronic memory, valleytronic devices

Posted Date: September 8th, 2020

DOI: <https://doi.org/10.21203/rs.3.rs-68366/v1>

License:   This work is licensed under a Creative Commons Attribution 4.0 International License.

[Read Full License](#)

Abstract

Analogous to conventional charge-based electronics, valleytronics aims at encoding data via valley degree of freedom, enabling new routes for information processing. Long-lived interlayer excitons (IXs) in van der Waals heterostructures (HSs) stacked by transition metal dichalcogenides (TMDs) carry valley-polarized information and thus would find promising applications in valleytronic devices. Although great progress of IX based valleytronic devices has been achieved, nonvolatile valleytronic memories are still challenging. Here, we demonstrate IX based nonvolatile valleytronic memory in a WS₂/WSe₂ HS. The emission characteristics of IX exhibit a large excitonic/valleytronic hysteresis upon cyclic-voltage sweeping. Importantly, IX emission can be electrically switched between a bright state and a dark state with large light-intensity and helicity contrast of about 1.7 and 1.8, respectively, which can be ascribed to the chemical-doping of O₂/H₂O redox couple between TMDs and substrate. Taking advantage of the large hysteresis, IX can be utilized for manipulating and nonvolatile storing valley information and IX based nonvolatile valleytronic memory has been successfully demonstrated. These findings open up an avenue for nonvolatile valleytronic memory and would motivate more investigations on valleytronic devices.

Background

Van der Waals HSs stacked by TMDs monolayers enable the generation of long-lived IXs with a large binding energy of about 150 meV¹, and a long diffusion distance over five micrometres², further extending the already appealing properties of the constituent TMDs monolayers. Since IXs are composed of electrons and holes that are resided in neighboring layers, their physical properties strongly depend on the layer configurations and external fields or dopings³⁻⁵. Through electrical field or doping, we can modulate the emission intensity and wavelength of the IX^{1,6}, and even switch its polarization⁷. Recently, IX in the HSs stacked by other layered materials such as 2D perovskites and InSe with TMDs monolayer has been demonstrated and can be utilized in mid-infrared photodetections and valleytronics^{8,9}. In particular, dark IX with a long lifetime exhibits unique merit in valleytronic devices. Nevertheless, the manipulation of dark exciton is hard and study on nonvolatile valleytronic memory remains elusive. In this work, we have successfully achieved nonvolatile valleytronic memory based on IX in TMDs HSs, which would greatly prompt relevant investigations on valleytronics.

The HS is formed by a monolayer WS₂ (top) and a monolayer WSe₂ (bottom), both of which are contacted with an electrode (Fig. 1a). By applying voltage between the electrode and the heavily-doped Si substrate, we can control the doping level of the device when performing optical measurements. Fig. 1b shows the optical microscopy image of the device. The WS₂ and WSe₂ sheets are mechanically exfoliated from their respective bulk crystals and then transferred on a SiO₂/p⁺⁺-Si substrate through dry-transfer technique¹⁰. The edges of the two sheets are intentionally aligned to improve interlayer coupling³.

IX in the WS₂/WSe₂ HS. Fig. 1c shows the PL spectra of the HS, from which we can observe a severe PL quenching and redshift of the intralayer excitonic peaks, together with the appearance of a low-energy peak at 1.4 eV. The quenching and redshift of the intralayer excitonic peaks can be attributed to the interlayer charge transfer^{11,12} and modified dielectric environment^{13,14}, respectively. We ascribe the peak at 1.4 eV to the emission of IX according to previous reports^{15,16}. The excitation-power dependent PL spectra further verify its interlayer nature (Fig. 1d). The IX emission peak shows a blueshift with the increase of excitation power, which is due to many-body effect arising from the repulsive interaction between the dipole-aligned IX^{4,17,18}.

Excitonic hysteresis of the IX. To explore gate-dependent features of the IX emission, we measured the PL spectra of the device under cyclic V_g, which scans first from 0 V to 60 V, then down to 0 V, then to -60 V, and finally back to 0 V (Fig. 2a). The IX emission peak shows a redshift and the emission intensity is enhanced with the decrease of V_g, and vice versa. The redshift of the IX emission peak with V_g can be ascribed to the Stark effect^{7,19}, which is further verified by the opposite shift trend of the IX emission peak in the devices with stacking order inversed (Fig. S1). Interestingly, the IX emission peak exhibits a strong hysteresis upon cyclic-voltage sweeping. As marked by black arrows in Fig. 2a, the peak position of the IX at middle 0 V (0V-2) cannot return to the same value of initial 0 V (0V-1), until a upward scanning and finally back to 0 V (0V-3). The gate-dependent photon energy and PL intensity can be seen more clearly in Fig. 2b and 2c. For a simple discussion, we only compare the states at 0V-2 and 0V-3. The photon energy of 0V-2 is blueshifted by about 20 meV with respect to that of 0V-3. Meanwhile, the PL intensity of 0V-2 is weaker than 0V-3 with a contrast ratio (I₃/I₂) of about 1.7. It is worth noting that the light intensity increases non-monotonously as V_g decreases from 0 V to -60 V, indicating the occurrence of chemical doping^{20,21}, which will be discussed in the following.

The IX emission peak of 0V-2 exhibits an asymmetric lineshape, which can be decomposed to two Gaussian peaks (Fig. 2d). The energy difference of the two peaks is about 20 meV that is consistent with the splitting energy of the conduction band of WS₂^{22,23}, strongly suggesting the occurrence of dark excitons. This peculiar phenomenon can be understood from the chemical-doping^{20,21} induced band-filling effect^{5,24}. Due to the type-II band alignment, electrically-doped electrons and holes reside only in the WS₂ and WSe₂ layer respectively, as illustrated in Fig. 2e and 2f. When the device is chemically n-doped, the Fermi level will be lift up and the IX will shift to a dark state (IX_D), which has an inefficient PL yield because of inversed spin in dark excitons. Contrarily, when the chemically-doped electrons are released, the IX will return to a bright state (IX_B). Therefore, the IX emission peaks in 0V-1 and 0V-3 spectra are attributed to bright-exciton emission, and that in 0V-2 spectra is resulted from dark exciton. The difference of light intensities between 0V-3 and 0V-1 might be due to different levels of chemical doping at the initial and final sweeping stages.

Mechanism of the excitonic hysteresis. Electrical hysteresis is very common in two-dimensional material devices, such as graphene and TMDs based field-effect transistors^{25,26}. Generally, electrical hysteresis is

attributed to the chemical-doping effect by doping species (O_2 and H_2O) that are bound at the device/substrate interface, and/or on the surface of the device²⁷⁻³⁰. In our case, we propose that the excitonic hysteresis mentioned above is originated from the same scenario. Since our measurements were performed in high vacuum ($\sim 10^{-7}$ Torr), the influence of the molecules on the device surface can be safely neglected. Therefore, the excitonic hysteresis is more likely due to the O_2/H_2O molecules that are trapped at the interface between the HS and substrate. To clarify this, we examine the gate-dependent PL spectra of the individual WSe_2 region (Fig. 3a), because WSe_2 is in the bottom of the HS and directly contacts the SiO_2/Si substrate. Additionally, we conducted a control experiment with WSe_2 monolayer on a hydrophobic substrate (Fig. 3b).

Interestingly, the emission features of the intralayer excitons in WSe_2 are closely correlated to that of IX. As V_g decreases from 0 V to -60 V, the emission of positive trions (X^+) is gradually enhanced, while the peak of neutral excitons (X_0) is suppressed, indicating an efficient hole doping (detailed data is provided in Fig. S2). Peculiarly, as V_g increases from -60 V back to 0 V, the evolution track is asymmetric to that from 0 V to -60 V. The trion emission peak is firstly weakened, then enhanced and redshifted with the increase of V_g . The asymmetric evolution strongly indicates the occurrence of negative trions X^- and suggests that the WSe_2 is chemically n-doped^{30,31} at 0V-2. When V_g increases from 0 V to 60 V, the peak is redshifted further, but with emission intensity weakened because of Coulomb screening from the free electrons³². When voltage scans backward from 60 V to 0 V, the peak shows a blueshift and emission intensity becomes weaker while the peak is gradually enhanced, indicating that the chemically-doped charges have been released. All the above features are well consistent with the previously mentioned chemical-doping induced band-filling mechanism.

To validate such speculation, we then focus on the PL spectra of a control device with monolayer WSe_2 on a hydrophilic substrate (Fig. 3b). The evolution track of X^+ and X_0 emission are roughly symmetric along the black dashed line at about -50 V. The slight deviation of the symmetry line at -50 V (rather than -60 V) might be due to trace O_2/H_2O molecules that are absorbed on WSe_2 before the transfer procedure. Besides, the track of X^- is symmetrical about the dashed line at 60 V. Such symmetric evolution suggests that the excitonic hysteresis is largely suppressed, thus proving the important role of H_2O in our observations. The broad PL peak centered at about 1.65 eV might be due to local-state exciton³³, which is out of the scope of this study.

The surface of SiO_2 is usually covered with a layer of silanol groups ($\equiv Si - OH$), especially after it is treated by piranha solution or plasma cleaner^{20,30}. With these silanol groups, SiO_2/Si substrates are easily bound by ambient O_2 and H_2O molecules³⁴. As shown in Fig. 3c, the electrochemical potential of the redox couple (O_2/H_2O) is about -5.3 eV^{20,35}, which is slightly higher than the valence band of WSe_2 (about -5.46 eV)^{36,37}. Electrons spontaneously transfer from O_2/H_2O to WSe_2 , making monolayer WSe_2 initially n-doped (detailed information is provided in Fig. S2), and resulting in the deviated symmetry at

-50 V in Fig. 3b. The applied negative gate voltages would force electrons further transferring from O_2/H_2O to WSe_2 . Those chemically-doped electrons balance out the gate modulation, resulting in the non-monotonic behavior of IX in $0 \sim -60$ V range (Fig. 2c) and the excitonic hysteresis. The chemical-doping effect also explains why emission maintains its intensity from 0 V to -60 V for WSe_2 on the hydrophilic substrate (Fig. 3a) but greatly suppressed on the hydrophobic substrate (Fig. 3b). When applying positive gate voltages, the chemical-doped charges are driven back from WSe_2 to the O_2/H_2O redox couple. As a consequence, the intralayer excitons of WSe_2 return to the initial state whereas the IX returns to the bright state. This control experiment further verifies the chemical-doping mechanism and well explains the origin of the excitonic hysteresis of IX shown in Fig. 2. To confirm the scenario, we made a WS_2/WSe_2 HS on a hydrophobic substrate, which shows no hysteresis (Fig. S3). In addition, we also fabricated a WS_2/WSe_2 /BN HS on a hydrophilic substrate with WS_2/WSe_2 HS partially separated from the substrate by a thin layer BN. For this device, the excitonic hysteresis is observed in the region where WS_2/WSe_2 HS directly contacts with substrate, but absent in the BN-insulated region, which further supports that the excitonic hysteresis originates from the interface trap states (Fig. S4).

Hysteresis of circular polarization degree of the IX. To study the chemical-doping effect on the chirality features of IX, we measured the helicity-resolved PL spectra of the device (Fig. 4a). Interestingly, the IX peak exhibits a negative circular polarization in contrast to that of intralayer excitons in WSe_2 and WS_2 , which can be ascribed to the interlayer quantum interference imposed by the atomic registry between the constituent layers³⁸. To qualify the valley polarization, the degree of circular polarization has been introduced, which can be defined as $P_C = (I^+ - I^-)/(I^+ + I^-)$, where I^+ (I^-) denotes the intensity of co-polarized (cross-polarized) PL component with the excitation. The IX peak exhibits $P_C = -12.3\%$, while the intralayer excitonic peak of WS_2 and WSe_2 shows $P_C = 15\%$ and 7.1% , respectively.

The valley polarization of IX can also be electrically controlled by V_g . As shown in Fig. 4b, the circular polarization rate shows strong voltage dependence (the full data set is provided in Fig. S5). The absolute polarization degree is greatly suppressed at -60 V (p-doping), but enhanced at 60 V (n-doping). Interestingly, the helicity of the IX emission also exhibits a strong hysteresis. The polarization degree of 0V-2 is much larger than that of 0V-1 and 0V-3. This observation further supports the presence of dark exciton^{7,39}, because it has a long lifetime that suppresses valley depolarization^{40,41}, as illustrated in Fig.4c and 4d. Due to long-range electron-hole exchange⁴⁰, electrons in the K valley are scattered from the conduction band to the valence band, whereas electrons in the K' valley are scattered from the valence band to the conduction band. This process can also be regarded as virtual recombination of an exciton in the K valley and generation of another exciton in the K' valley, or vice versa. The long-range electron-hole exchange typically takes a few picoseconds⁴¹, and the lifetime of the bright and dark IX is about several nanoseconds and microseconds³⁹, respectively. Therefore, the valley depolarization is strong for bright IX (Fig. 4c) but largely suppressed for long-lived dark IX (Fig. 4d). As a result, the IX can be switched between the bright and dark states by cyclic V_g , leading to the presence of the hysteresis of circular polarization degree. We define the helicity contrast as H_C , where $H_C = (P_C^+ - P_C^-)/P_C$ and P_C is the circular polarization degree of

0V-2 and 0V-3 state, respectively. The helicity contrast is about 1.8, indicating potential application of valleytronic information processing and storage.

IX based valleytronic memory.

Due to the strong interaction with light, exciton-based information can be detected by photon energy, PL intensity and chirality contrast through optical approaches. To demonstrate the valley-encoding ability of the device, we measured the time-dependent PL spectra under circular excitation (σ), as shown in Fig. 5a. As gate voltage cyclically changes among -60 V, 0 V, 60 V and 0 V, the photon energy of the IX emission periodically shifts among 1.38 eV, 1.42 eV, 1.45 eV, and 1.40 eV, which are analogous to the performance of conventional electronic devices under “write”, “read” and “erase” operations. In addition, the emission intensity also periodically changes in response to those memory operations. Specifically, the PL intensity of the bright state (1.40 eV) and the dark state (1.42 eV) can be utilized for information storage, because the intensity levels can persist for a long time with no power consumption. Intriguingly, as the detection helicity switches between σ and $-\sigma$, the PL intensity of the 0 and 1 states exhibit helicity-resolved features. There are four intensity levels emerged, which can be defined as “00”, “01”, “10” and “11”, indicating valley-encoding abilities of the device. Based on this feature, we can selectively encode/address the valley-polarized information by helicity excitation/ detection.

To evaluate the retention time of the encoded information, we then prolong the reading-operation time, as shown in Fig. 5b. Surprisingly, the 1 and 0 excitonic states can persist for at least 60 minutes, holding great promise for nonvolatile valleytronic memories. As a matter of fact, the retention time should be much longer than 60 minutes, as can be seen in a logarithmic-timescale plot (Fig. S6a). We also note that the 0 (1) state varies dynamically before reaching a steady state. This is probably due to the charging/discharging process of the device, as confirmed by the features of time-dependent leakage current (Fig. S6b). More important, the information encoding ability of the device can persist up to 250 K, which shows great promising for high temperature valleytronic devices (supplementary materials Fig. S7).

Conclusions

In summary, we have systematically investigated the excitonic/valleytronic hysteresis of IX in a WS_2/WSe_2 HS. By examining the PL spectra of the WSe_2 monolayers on hydrophilic and hydrophobic substrates, we verify that the origin of the hysteresis is the chemical-doping of WSe_2 by O_2/H_2O redox couple. Benefit from the hysteresis effect, IX can be electrically switched between a dark state and a bright state with large PL intensity and helicity contrast of about 1.7 and 1.8 respectively. Such intriguing feature holds great promise for nonvolatile memory in excitonic and valleytronic applications. Finally, we demonstrate the memory function of the device, which shows a good writing/reading/erasing ability with retention time exceeding 60 minutes. Importantly, the nonvolatile IX-based data hold valley-polarized information, which may greatly motivate the development of valleytronic science and applications.

Further, this work provides a convenient approach for the manipulation of dark exciton that features longer lifetime and larger valley-polarized degree than common bright exciton.

Methods

Sample Preparations. Electrodes were fabricated by standard photolithography and thermal evaporation (50 nm/2 nm Au/Cr). The substrates with prefabricated electrodes are ultrasonic cleaned and plasma cleaned before the fabrication of the HS. WS_2 and WSe_2 monolayer flakes were first mechanically exfoliated onto polymethyl-methacrylate (PMMA) stamps, and then transferred on a SiO_2 (300 nm)/Si wafer using a dry transfer technique with the aid of an optical microscope and a nano-manipulator. The hydrophobic substrates were prepared via immersed in HMDS vapor for 10 min and then rinsed with acetone for 30 s to form a hydrophobic layer on the substrate⁴².

Optical Measurements. The as-fabricated devices were mounted in a continuous flow cryostat with 10^{-7} Torr vacuum. All the measurements were conducted at 78 K. For gate-dependent PL measurement, the sample was excited by a 532 nm laser with 23 μW . For the helicity-resolved PL measurement, the sample was excited by a 633 nm laser with a power of 180 μW . The time interval between two adjacent spectra is about 1 min when performing gate-dependent measurement. For the memory operation measurement, the spectra were acquired with V_g changing cyclically and laser keeping focused on the sample. Each spectrum was measured within 10 seconds. All the PL spectra were collected by a 50 \times objective lens (N.A. = 0.7) in a Raman spectrometer (Horiba HR550) with a 600 g/mm grating. A Keithley 2400 sourcemeter was used as the voltage source.

Declarations

The authors declare no competing financial interest.

ACKNOWLEDGMENT

D. L. acknowledges the support from National Key Research and Development Program of China (2018YFA0704403), NSFC (61674060) and Innovation Fund of WNLO.

References

1. Jauregui, L. A. *et al.* Electrical control of interlayer exciton dynamics in atomically thin heterostructures. *Science* **366**, 870 (2019).
2. Unuchek, D. *et al.* Room-temperature electrical control of exciton flux in a van der Waals heterostructure. *Nature* **560**, 340 (2018).
3. Nayak, P. K. *et al.* Probing Evolution of Twist-Angle-Dependent Interlayer Excitons in $\text{MoSe}_2/\text{WSe}_2$ van der Waals Heterostructures. *ACS Nano* **11**, 4041 (2017).

4. Rivera, P. *et al.* Observation of long-lived interlayer excitons in monolayer MoSe₂-WSe₂ heterostructures. *Nat. Commun.* **6**, 6242 (2015).
5. Ciarrocchi, A. *et al.* Polarization switching and electrical control of interlayer excitons in two-dimensional van der Waals heterostructures. *Nat. Photonics* **13**, 131–136 (2019).
6. Rivera, P. *et al.* Valley-polarized exciton dynamics in a 2D semiconductor heterostructure. *Science* **351**, 688 (2016).
7. Ciarrocchi, A. *et al.* Polarization switching and electrical control of interlayer excitons in two-dimensional van der Waals heterostructures. *Nat. Photonics* **13**, 131 (2019).
8. Ubrig, N. *et al.* Design of van der Waals interfaces for broad-spectrum optoelectronics. *Nat. Mater.* **19**, 299 (2020).
9. Chen, Y. *et al.* Robust Interlayer Coupling in Two-Dimensional Perovskite/Monolayer Transition Metal Dichalcogenide Heterostructures. *ACS Nano*, doi:10.1021/acsnano.0c03624 (2020).
10. Castellanos-Gomez, A. *et al.* Deterministic transfer of two-dimensional materials by all-dry viscoelastic stamping. *2D Mater.* **1**, 011002 (2014).
11. Jin, C. *et al.* Ultrafast dynamics in van der Waals heterostructures. *Nat. Nanotechnol.* **13**, 994 (2018).
12. Hong, X. *et al.* Ultrafast charge transfer in atomically thin MoS₂/WS₂ heterostructures. *Nat. Nanotechnol.* **9**, 682 (2014).
13. Kumar, R. *et al.* Interlayer screening effects in WS₂/WSe₂ van der Waals hetero-bilayer. *2D Mater.* **5** (2018).
14. Raja, A. *et al.* Coulomb engineering of the bandgap and excitons in two-dimensional materials. *Nat. Commun.* **8**, 15251 (2017).
15. Jin, C. *et al.* Identification of spin, valley and moiré quasi-angular momentum of interlayer excitons. *Nat. Phys.* **15**, 1140 (2019).
16. Ye, T., Li, J. & Li, D. Charge-Accumulation Effect in Transition Metal Dichalcogenide Heterobilayers. *Small* **15**, 1902424 (2019).
17. Butov, L. V., Lai, C. W., Ivanov, A. L., Gossard, A. C. & Chemla, D. S. Towards Bose–Einstein condensation of excitons in potential traps. *Nature* **417**, 47 (2002).
18. Nagler, P. *et al.* Interlayer exciton dynamics in a dichalcogenide monolayer heterostructure. *2D Mater.* **4**, 025112 (2017).
19. Wang, T. *et al.* Giant Valley-Zeeman Splitting from Spin-Singlet and Spin-Triplet Interlayer Excitons in WSe₂/MoSe₂ Heterostructure. *Nano Lett.* **20**, 694 (2020).
20. Xu, H., Chen, Y., Zhang, J. & Zhang, H. Investigating the mechanism of hysteresis effect in graphene electrical field device fabricated on SiO₂ substrates using Raman spectroscopy. *Small* **8**, 2833 (2012).
21. Liu, H. *et al.* Two-Dimensional WSe₂/Organic Acceptor Hybrid Nonvolatile Memory Devices Based on Interface Charge Trapping. *ACS Appl. Mater. Interfaces* **11**, 34424 (2019).

22. Echeverry, J. P., Urbaszek, B., Amand, T., Marie, X. & Gerber, I. C. Splitting between bright and dark excitons in transition metal dichalcogenide monolayers. *Phys. Rev. B* **93**, 121107 (2016).
23. Eickholt, P. *et al.* Spin Structure of K Valleys in Single-Layer WS₂ on Au(111). *Phys. Rev. Lett.* **121**, 136402 (2018).
24. Jones, A. M. *et al.* Spin–layer locking effects in optical orientation of exciton spin in bilayer WSe₂. *Nat. Phys.* **10**, 130 (2014).
25. Ye, T. *et al.* Approaching the Intrinsic Lifetime and Modulating a Graphene Plasmonic Resonance at a Few Hundred GHz. *Adv. Opt. Mater.* **7**, 1900315 (2019).
26. Urban, F. *et al.* Gas dependent hysteresis in MoS₂ field effect transistors. *2D Mater.* **6**, 045049 (2019).
27. Late, D. J., Liu, B., Matte, H. S. S. R., Dravid, V. P. & Rao, C. N. R. Hysteresis in Single-Layer MoS₂ Field Effect Transistors. *ACS Nano* **6**, 5635–5641 (2012).
28. Shu, J. *et al.* The intrinsic origin of hysteresis in MoS₂ field effect transistors. *Nanoscale* **8**, 3049 (2016).
29. Kaushik, N. *et al.* Reversible hysteresis inversion in MoS₂ field effect transistors. *npj 2D Mater. Appl.* **1**, 34 (2017).
30. Park, K., Kang, H., Koo, S., Lee, D. & Ryu, S. Redox-governed charge doping dictated by interfacial diffusion in two-dimensional materials. *Nat. Commun.* **10**, 4931 (2019).
31. Zheng, L. *et al.* Reversible n-Type Doping of Graphene by H₂O-Based Atomic-Layer Deposition and Its Doping Mechanism. *J. Phys. Chem. C* **119**, 5995 (2015).
32. Chernikov, A. *et al.* Electrical Tuning of Exciton Binding Energies in Monolayer WS₂. *Phys. Rev. Lett.* **115**, 126802 (2015).
33. Shang, J. *et al.* Observation of Excitonic Fine Structure in a 2D Transition-Metal Dichalcogenide Semiconductor. *ACS Nano* **9**, 647–655 (2015).
34. Zhuravlev, L. T. The surface chemistry of amorphous silica. Zhuravlev model. *Colloids Surf. A Physicochem. Eng. Asp.* **173**, 1–38 (2000).
35. Chakrapani, V. *et al.* Charge Transfer Equilibria Between Diamond and an Aqueous Oxygen Electrochemical Redox Couple. *Science* **318**, 1424 (2007).
36. Wang, K. *et al.* Electrical control of charged carriers and excitons in atomically thin materials. *Nat. Nanotechnol.* **13**, 128 (2018).
37. Li, X. *et al.* Graphene and related two-dimensional materials: Structure-property relationships for electronics and optoelectronics. *Appl. Phys. Rev.* **4**, 021306 (2017).
38. Hsu, W. T. *et al.* Negative circular polarization emissions from WSe₂/MoSe₂ commensurate heterobilayers. *Nat. Commun.* **9**, 1356 (2018).
39. Jiang, C. *et al.* Microsecond dark-exciton valley polarization memory in two-dimensional heterostructures. *Nat. Commun.* **9**, 753 (2018).

40. Yu, T. & Wu, M. W. Valley depolarization due to intervalley and intravalley electron-hole exchange interactions in monolayer MoS₂. *Phys. Rev. B* **89**, 205303 (2014).
41. Yang, M. *et al.* Exciton valley depolarization in monolayer transition-metal dichalcogenides. *Phys. Rev. B* **101**, 115307 (2020).
42. Li, L. *et al.* Two-Step Growth of 2D Organic-Inorganic Perovskite Microplates and Arrays for Functional Optoelectronics. *J Phys. Chem. Lett.* **9**, 4532 (2018).

Figures

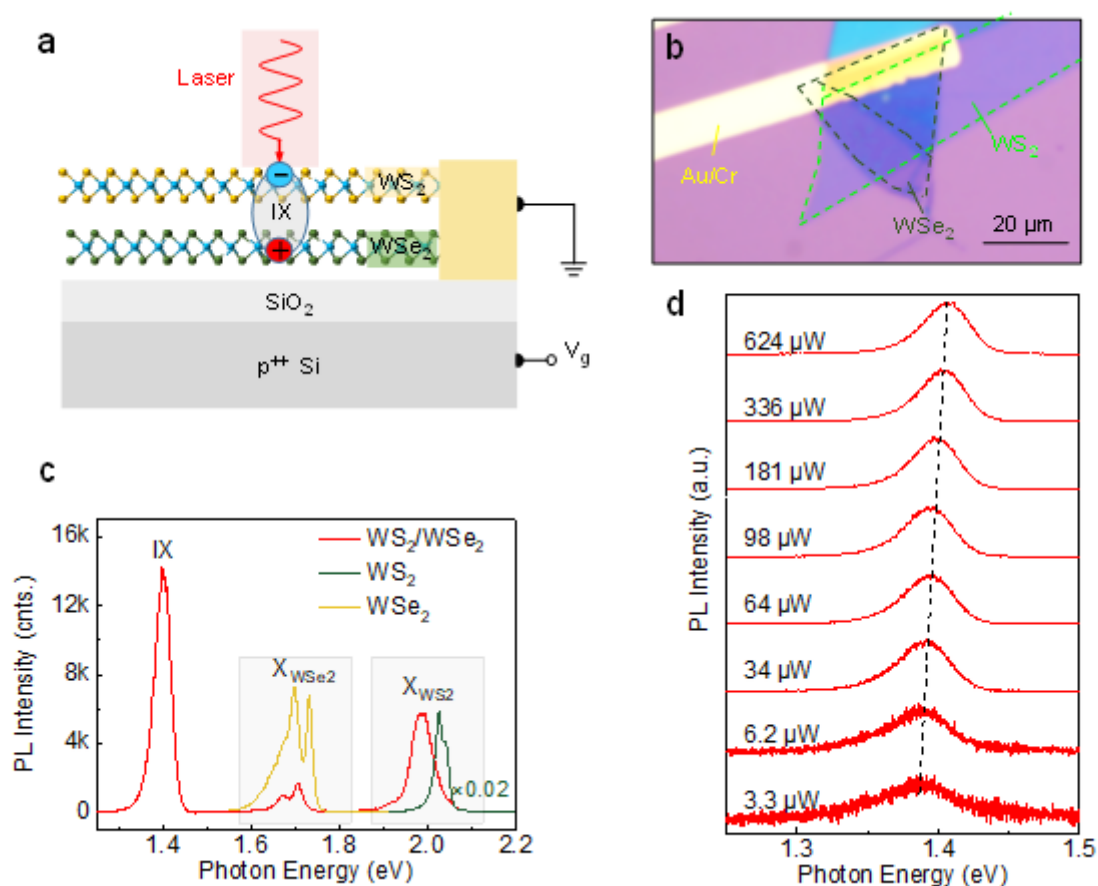


Figure 1

IX in an electrically-tunable WS₂/WSe₂ HS. a-b, Schematic and optical microscopy image of the device. c, PL spectra of the HS. d, PL spectra of the IX as a function of excitation power. The spectra are vertically shifted for clarity.

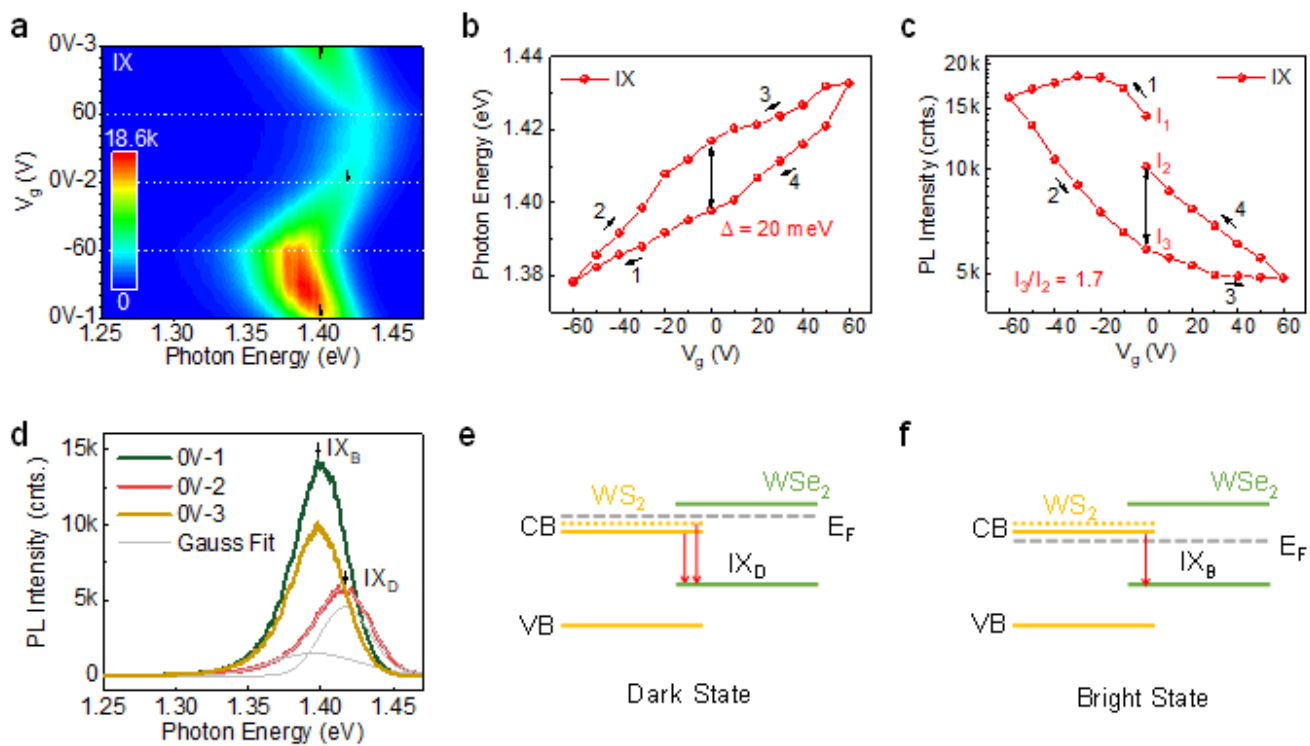


Figure 2

Electrical control of the IX emission. a, Contour plot for the PL spectra of IX upon cyclic V_g . White dashed lines serve as guides to the eye. Black arrows mark the peak positions of the IX at 0 V with different scanning sequences. b-c, Photon energy and PL intensity of the IX as a function of V_g . d, PL spectra of the IX at 0 V with different scanning sequences. 0V-1, 0V-2 and 0V-3 represent three spectra marked in a. Gray lines are Gaussian fits to the 0V-2 spectrum. e-f, Schematic of the bright and dark excitons. Chemical-doped electrons lift the Fermi level up and shift the IX to a dark state (IX_D). When those electrons are released, the IX returns to a bright state (IX_B). The orange dashed line stands for the upper spin-splitting conduction band (CB) of WS₂. Red arrows represent the recombination paths of the IX.

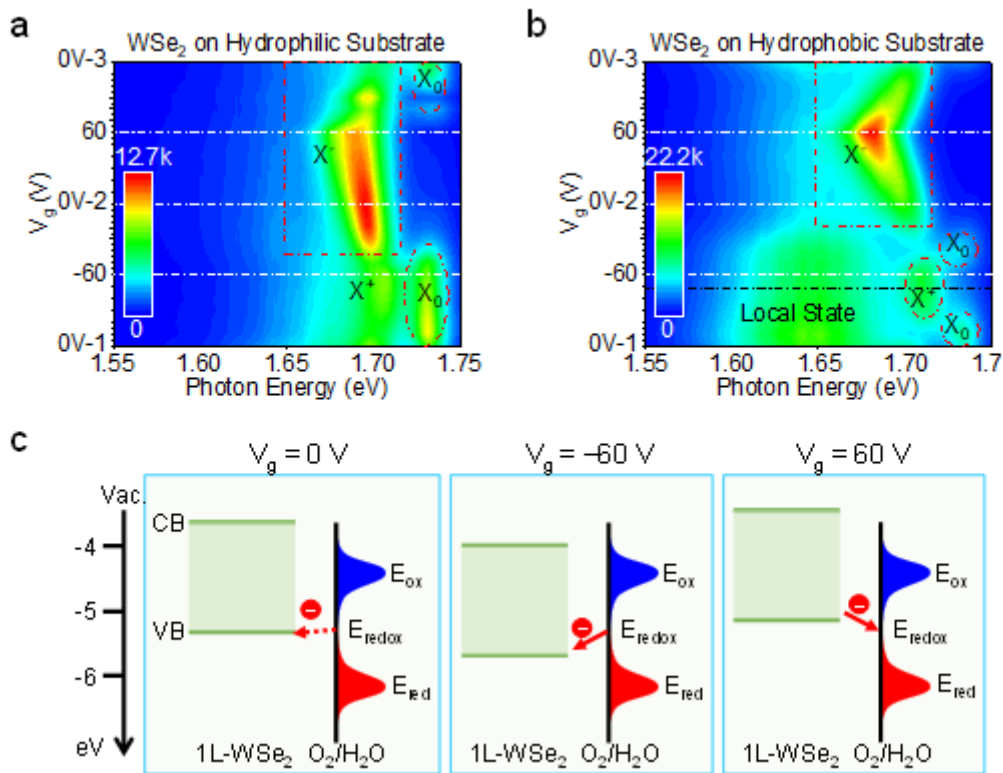


Figure 3

Mechanism of the excitonic hysteresis. (a) Contour plot for the PL spectra of WSe₂ as a function of cyclic V_g . The spectra were acquired in the individual WSe₂ region of the HS on a hydrophilic substrate. (b) Contour plot for the PL spectra of monolayer WSe₂ on a hydrophobic substrate, which is functionalized by hexamethyldisilazane (HMDS). The black dashed line indicates the symmetric position of the evolution track of X^{+} and X_0 . (c) Illustration of chemical doping caused by O₂/H₂O molecules. The electronic density of states (DOS) reflect the electron energy distribution around the oxidation potential (E_{ox}) and reduction potential (E_{red}), respectively.

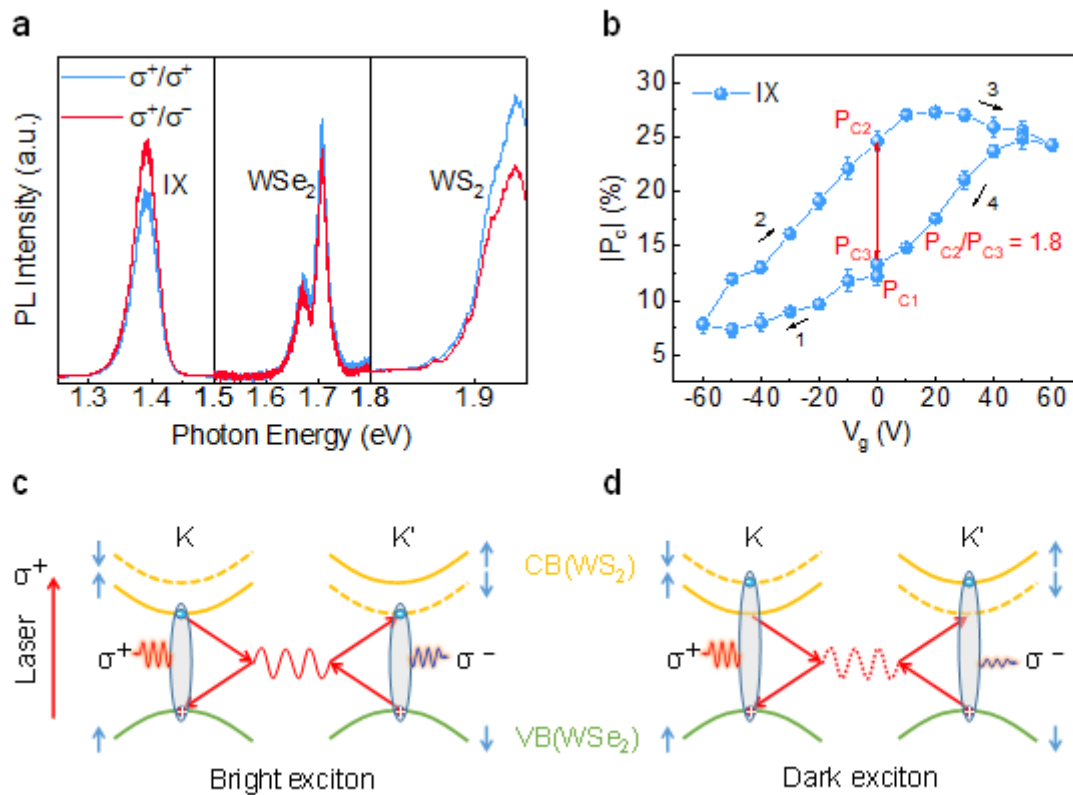


Figure 4

Electrically-tunable valley polarization of IX. a, Helicity-resolved PL spectra of the HS under 633 nm excitation at 78 K. b, Absolute circular polarization degree of IX as function of V_g. c-d, Schematic diagram of intervalley scattering between the K and K' valleys for bright and dark IXs. The intervalley transition is caused by the virtual recombination of an exciton in the K valley and then generation in the K' valley, or vice versa. Due to a long lifetime, the valley depolarization of dark IX is largely suppressed.

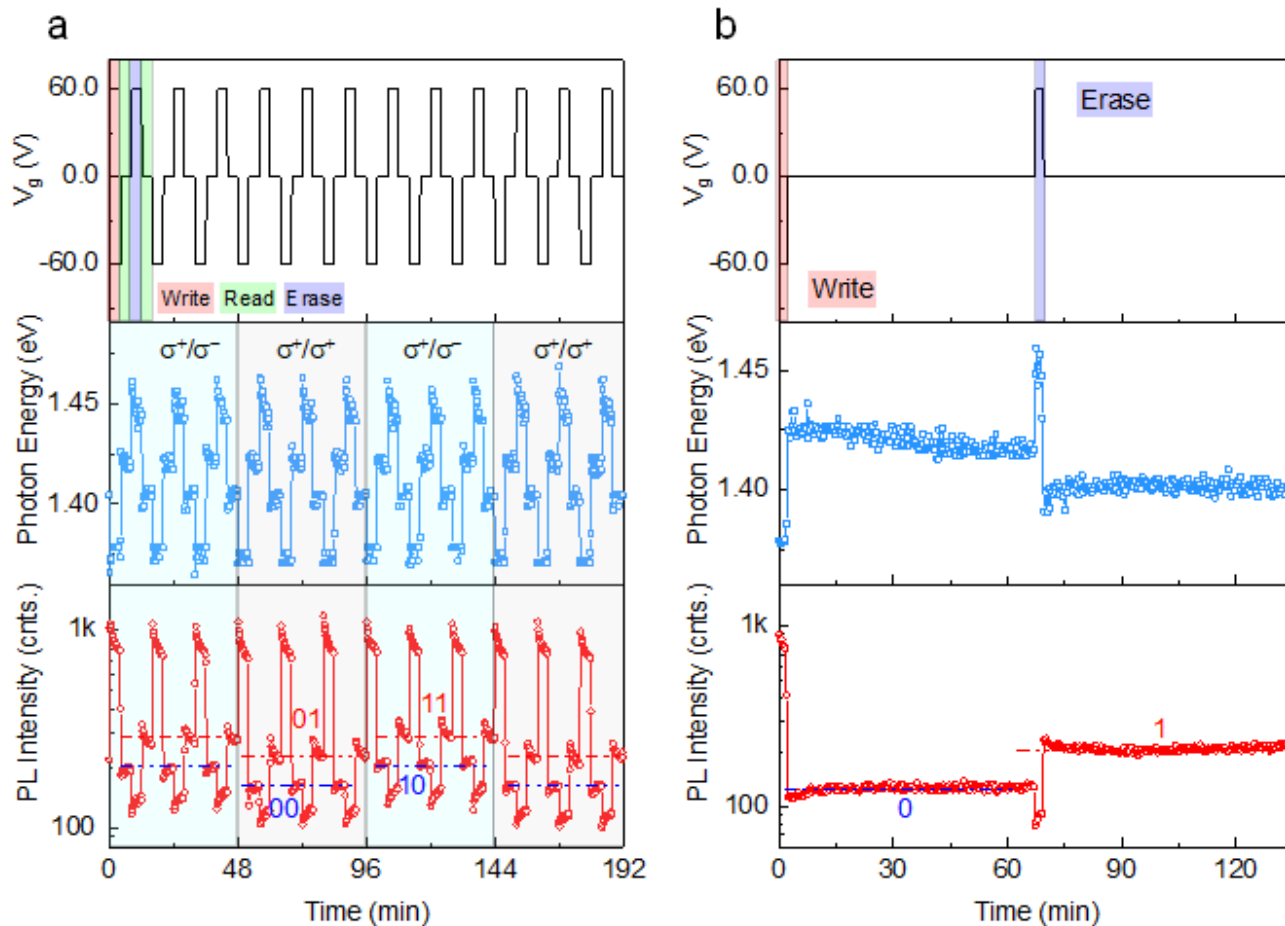


Figure 5

Nonvolatile valleytronic memory operation in the HS. a, Time-dependent IX emission characteristics upon cyclic V_g among -60 V, 0 V, 60 V and 0 V. Each voltage last for about 4 minutes. The detecting polarization shifts every three cycles of V_g . b, Retention time of the “1” and “0” excitonic states. The writing and erasing voltages last for about 3 minutes, and the reading voltage lasts for about 64 minutes. The peak energies and intensities are extracted from real-time spectra, each of which was measured within 10s.

Supplementary Files

This is a list of supplementary files associated with this preprint. Click to download.

- [SupportingMaterialsV2.docx](#)